

Full Length Article

In situ defect detection in selective laser melting via full-field infrared thermography

Jamison L. Bartlett^a, Frederick M. Heim^a, Yellapu V. Murty^b, Xiaodong Li^{a,*}^a Department of Mechanical and Aerospace Engineering, University of Virginia, 122 Engineer's Way, Charlottesville, VA, 22903, USA^b MC Technologies, Charlottesville, VA, 22901, USA

ARTICLE INFO

Keywords:

Additive manufacturing
Infrared thermography
Process monitoring
Selective laser melting
Defects

ABSTRACT

Selective laser melting (SLM) has become one of the most commonly utilized processes in metal additive manufacturing (AM). Despite its widespread use and capabilities, SLM parts are still being produced with excessive volumetric defects and flaws. The complex dependence of defect formation on process parameters, geometry, and material properties has inhibited effective quality assurance in SLM production. Exacerbating these issues are the difficulties thus far in accurately detecting and identifying defects in-process so that parts may be qualified without destructive testing. Some of the most detrimental defects produced during SLM processing are lack of fusion (LoF) defects, which are frequently found to be in excess of 100 μm in size, thus these defects are of critical importance to detect and remove. In this work, we have developed and demonstrated the capabilities of a novel *in situ* monitoring system using full-field infrared (IR) thermography to monitor AlSi10Mg specimens during SLM production. Using layerwise relative surface temperature measurements, subsurface defects were identified via their retained thermal signature at the surface; transient thermal modeling was performed, which supported these observations. Parts were characterized using *ex situ* scanning electron microscopy (SEM) to validate data identified defects and, critically, to estimate detection success. The IR defect detection method was highly effective in identifying defects, with an 82% total success rate for LoF defects; detection success improved with increasing defect size. The method was also used statistically to analyze the presence of systematic process errors during SLM production, expanding the capabilities of IR monitoring methods. This unique analysis method and simple integration for *in situ* IR monitoring can immediately improve non-destructive qualification methods in SLM processing.

1. Introduction

Selective laser melting (SLM) has grown rapidly in recent years and has become one of the most prominent additive manufacturing (AM) methods in industry. AM of metals brings the potential to rapidly produce parts with complex geometries in a single production step [1]. SLM processing, due to intense thermal gradients and cooling rates, generally results in fine grained microstructures, which typically produces parts that are mechanically equivalent or superior to their cast counterparts under static loading [2].

However, due to the challenging processing conditions, several challenges also arise in SLM which result in uncertainties in part qualification that have severely hindered its widespread acceptance [3]. The selectively melted (and layer by layer) nature of the SLM process can result in local or global anisotropy [4], large residual stresses [5] and a wide range of material defects [1] that may critically affect

mechanical properties [6]. Small, finely dispersed, pores on the order of $\sim 10\text{--}30\ \mu\text{m}$ may occur from gas formation or entrapment in the melt [7,8]. Larger and irregularly shaped pores may additionally form due to a number of sources, including keyhole porosity caused by an excessively high powered, and/or slow, laser raster [9] and lack of fusion (LoF) defects formed due to a variety of process/laser anomalies including insufficient raster track overlap [10,11]. LoF defects may be the most critically debilitating to part performance; these defects can be large, filled with un-sintered powder, and of irregular geometry with sharp, stress concentrating, features that may severely limit fatigue life and fracture toughness. [1,12,13]. Furthermore, defect formation is highly dependent on process parameter selection, geometry and material properties [7,14–16]. Effective detection and monitoring of defects in-process is therefore necessary to ensure part reliability and quality for critical applications.

Past research in the literature for *in situ* monitoring has placed

* Corresponding author.

E-mail address: xl3p@virginia.edu (X. Li).<https://doi.org/10.1016/j.addma.2018.10.045>

Received 25 July 2018; Received in revised form 29 October 2018; Accepted 29 October 2018

Available online 01 November 2018

2214-8604/ © 2018 Elsevier B.V. All rights reserved.

strong emphasis on pyrometry, including infrared (IR) monitoring, because of the known part-process dependencies on thermal conditions [8,17]. Typically, *in situ* IR measurements have been used to monitor melt pool geometry and temperature, which can facilitate defect prediction from melt pool monitoring or the computational modeling of microstructural features. However, these melt pool methods for defect detection generally require significant and costly integration with machine laser optics [18–20] and usually require extremely high acquisition rates on the order of 10 kHz to track the highly dynamic temperature fluctuations [19]. Full-field imaging that utilizes lower frame rate captures with lesser data storage requirements may facilitate more expedient calculations that could lead to attainable real-time analysis. Furthermore, measurements of absolute temperatures demand difficult assessments of background radiation and material emissivity [21–23]. Optical image monitoring has also been performed in pursuit of defect detection wherein individual images were analyzed for discrepancies in parts, while generally being qualitative [24–26]; discrete distortion and temperature measurements have also been made in-process [27,28]. Raplee et al. used IR imaging to observe temperature distributions in electron beam melting (EBM) and alluded to the potential to identify process defects through these measurements, though they did not attempt to identify them in their study [29]. IR methods (including EOS's developed optical tomography system) for identifying process abnormalities have been well-documented in the literature, however the results have generally been analyzed without regard to the physical resulting defects [24–26]. Therefore, despite the understanding that IR imaging may facilitate defect detection, critical questions remain with regards to IR defect monitoring in PBF processing: 1) Do IR abnormalities in fact correlate to physical defects? 2) If so, with what confidence and what do the thermal signatures look like? 3) What types of material defects are identifiable with IR detection? 4) What are the limitations of detection for a given imaging setup? An additional question is also raised: can the layerwise data be analyzed cumulatively to ascertain additional information of process consistency, beyond individual layer analyses? This study aims to address each of these critical questions, which have not been reported elsewhere in the literature. This type of understanding, formed by answering these questions, is necessary in order to push current IR monitoring methods towards real-time process control and optimization, beyond the current state of IR monitoring which results only in qualitative displays of process irregularities that are open to interpretation.

To our knowledge, no study has been reported which has directly addressed these lingering questions through comparison of in-process full-field IR data to physical defects in SLM processing. To begin to answer these critical questions, we employ a new and facile strategy for *in situ* process monitoring using full-field IR thermography of entire layers (as opposed to melt-pool monitoring) to identify material defects in SLM processing and directly evaluate the system's capabilities through *ex situ* characterization. This was accomplished by full-field IR measurements of part surfaces on a layer-by-layer basis, using *relative* temperature measurements during cool-down. We hypothesize that these full-field thermal images can enable direct identification of process induced subsurface defects, such as lack of fusion defects. Note that we define subsurface porosity as a pore below the exposed free surface and fully enclosed (not surface roughness or an open-ended pore) at any distance below the surface. We posit that lack of fusion defects, or other process induced subsurface porosity (likely with un-sintered powder and/or retained atmospheric gas), will reduce thermal conductivity in the vicinity and will thus retain heat in the region, which can be detected at the surface by thermal imaging. Driven by this hypothesis, we have integrated an infrared camera into an active SLM machine for evaluation. In-process data was analyzed throughout the build, and defect identification schemes were developed. IR identified anomalies through the build were further analyzed statistically to infer the presence of systematic SLM processing errors, demonstrating additional unreported capabilities of IR monitoring. Data determined process

defects were verified by *ex situ* characterization using scanning electron microscopy (SEM) to provide estimates of detection success rates for both LoF and keyhole defects.

2. Experimental methods

2.1. Machine integration

A long wave infrared (LWIR) camera was integrated into a Concept Laser X-line 1000R SLM machine during active production of parts. The camera was mounted overhead outside of the build chamber, viewing through a germanium window (suitable for LWIR) providing an unobstructed view of the top surface of the parts. The camera field of view covered a large section of the build plate, roughly 250 mm x 250 mm. No emissivity or background irradiance calibrations were performed, since only *relative* temperatures were required for the defect detection method developed.

2.2. Experimental processing conditions

To evaluate the capabilities of the IR system to detect defects in-process, and to preliminarily investigate process condition effects on defect formation, an experimental build was performed using the X-line 1000R SLM machine with IR monitoring. IR images were acquired from the start of the raster through initial cool-down at 7 frames per second. IR camera and software specifications are given in Table 1. Using this low frame rate acquisition, higher resolution images could be acquired within reasonable data storage limitations.

AlSi10Mg was selected for analysis, and powder was supplied by Valimet, U.S.A.; AlSi10Mg is currently the most commonly used aluminum alloy in SLM processing, with high Si content and good fluidity the alloy is not prone to cracking, and generally prints well with good resulting static mechanical properties [30,31]. Four cylindrical specimens 20 mm in diameter and 6 mm tall were produced within the field of view on an Al6061 build plate. The layer height was prescribed as 50 μ m, resulting in 120 layers for part completion. Cylindrical specimens were chosen to maximize surface area on the top of the parts for analysis while also providing axisymmetry and a direct axial conduction path at every position. The part axisymmetry eliminates geometric bias and allows for more rigorous investigation of process phenomena. Specimens were produced not to evaluate the success of different processing parameters, rather only to produce a large number (and varying sizes) of defects to compare to IR thermal data. Each of the four cylinders were produced with different laser parameters created to intentionally induce a range of defect frequencies and sizes. A baseline set, as developed through extensive past investigations by the machine technicians at our collaborating facility (Volunteer Aerospace in Knoxville, TN), was used to create a part with the best conditions available. A keyhole melting parameter set was used to create keyhole porosity, while a third parameter set was used to intentionally induce a large number of lack of fusion defects by reducing raster overlap. The final parameter set was created to produce spatter (material ejection) from the part. The result of this parameter set, in terms of defect production, was to produce only large lack of fusion defects. Therefore, since the mechanics of defect formation with changing process

Table 1
IR camera and software specifications.

Parameter	Specification
Camera	ICI FM-320P
Wavelength	Long wave (8–14 μ m)
Temperature range	– 20–650 °C
Acquisition software	IRFlash
Acquisition rate	7 fps
Acquisition time	~ 10 s/layer

Table 2
Laser build parameter sets utilized.

Parameter set	Laser power	Scan velocity
1. “Baseline”	350 W	1750 mm/s
2. “Keyhole Melting”	500 W	500 mm/s
3. “Lack of Fusion-1”	1000 W	2200 mm/s
4. “Lack of Fusion-2”	1000 W	1800 mm/s

parameters is not the focus of this study, this parameter set is simply denoted as “Lack of Fusion-2”. For all specimens a standard raster pattern was adopted utilizing vertical raster strips. While the pattern was not rotated between layers, it was translated horizontally every layer to avoid unnatural build-up of defects in preferred locations. Relevant laser parameters used for each part are given in Table 2; the geometry, position of the parts during production, and laser raster strategy is shown in Fig. 1.

2.3. Ex situ material characterization

Validation of data identified defects was conducted via scanning electron microscopy (SEM). The experimental specimens were each sectioned at 3 separate vertical planes using a low speed water-cooled diamond saw. Each cross-section was polished following standard metallographic procedures, and the parts were characterized using a FEI Quanta 650 SEM. Within each cross-section, a minimum of 3–5 randomly chosen defects were identified, imaged, and their centroidal x,y coordinates were determined within the SEM at the time of imaging and recorded for later comparison to in-process data identified anomalies. This characterization resulted in the locations of 10–20 defects being identified and randomly selected (without referring to IR data), ranging in size from 20 μm to greater than 500 μm , for each specimen, which were then compared to the locations of IR irregularities; this analysis resulted in direct comparisons of IR data to over 50 physical defects, allowing for initial detection success rates to be established. Success in detection was defined by the presence of a concentrated group of IR abnormalities (pixels with abnormal irradiance outside the standard deviation), covering at minimum the physical size of the defect observed via SEM, at the known physical defect location determined by SEM.

3. Defect identification and analysis methods

3.1. Infrared image processing

IR images acquired in-process were analyzed for defects using MATLAB R2017B software. The acquisition approach (7 fps capture) assumes that thermal signatures of subsurface defects are present and

remain on the part surface at this time scale ($\frac{1}{7}$ s). This strategy resulted in over 7000 IR images being captured through the 120-layer build. Therefore, it was necessary to establish strategies to select optimal images for analysis for each part and for each layer. Timestamp meta data was first used to group images within each layer of the build; then, images associated with the initial cool-down were identified for each part. The four parts were rastered sequentially in-process, therefore different images are required for the optimal analysis of each part. The end of the raster was signified by both a contour scan around the circumference and by the surrounding powder bed immediately adjacent to the part having higher mean irradiance than the part center; the powder bed retained heat since conduction was significantly reduced compared to that of the bulk metal. We leveraged this fact to identify the point in time when the raster had just been completed. We also include an additional criterion that the mean irradiance within the part must be set above a minimum relative value, determined empirically, which prohibited the premature selection of images before rastering had occurred. While this value was determined empirically post-process in this study, the value could also be automatically estimated (and refined through deposition) in-process by evaluating background irradiance levels, enabling real-time defect detection. With these criteria, we were able to successfully identify the start of the cool-down regime for each of the four parts in each of the 120 layers, reducing more than 7000 images to 480 (1 image per part x 4 parts x 120 layers) for analysis.

Analyzing the selected images, we then search for anomalies in irradiance within the part surface greater than ± 1 standard deviation away from the mean value. This simple criterion allowed for the identification of abnormal thermal signatures indicative of subsurface defects, which could then be further analyzed and compared to physical defects. Fig. 2 shows the method for processing images and determining thermal irregularities in parts during SLM processing.

3.2. Thermal modeling

To better understand the expected thermal signature produced by the presence of subsurface porosity, transient thermal modeling was conducted using ANSYS v19.2 software as a complement to experimental IR data. The cylindrical geometry was modeled with one layer left to be deposited (a completed height of 5.95 mm). A cylindrical pore 1 mm in diameter (xy plane) and 250 μm in height (build direction) was placed at an arbitrary location on the part surface and extended into both the completed underlying part and the next layer (25 μm into the new layer, and 225 μm downward into the completed part). The pore size was selected based on SEM imaging of the parts (Section 4.1). The underlying completed part was given an arbitrary equilibrium temperature of 200 $^{\circ}\text{C}$ prior to the addition of the final layer. In reality a thermal gradient existed through the part in the vertical/build

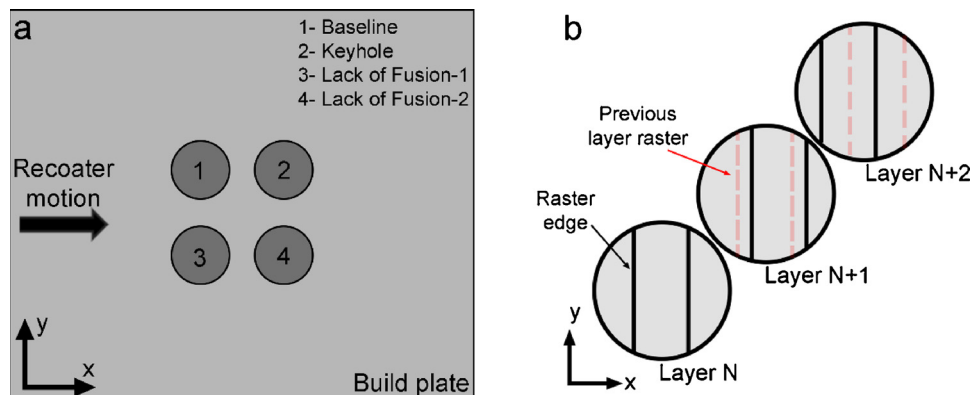


Fig. 1. Processing conditions of experimental specimens: a) part positions and established coordinate system and b) raster pattern and translation used between layers.

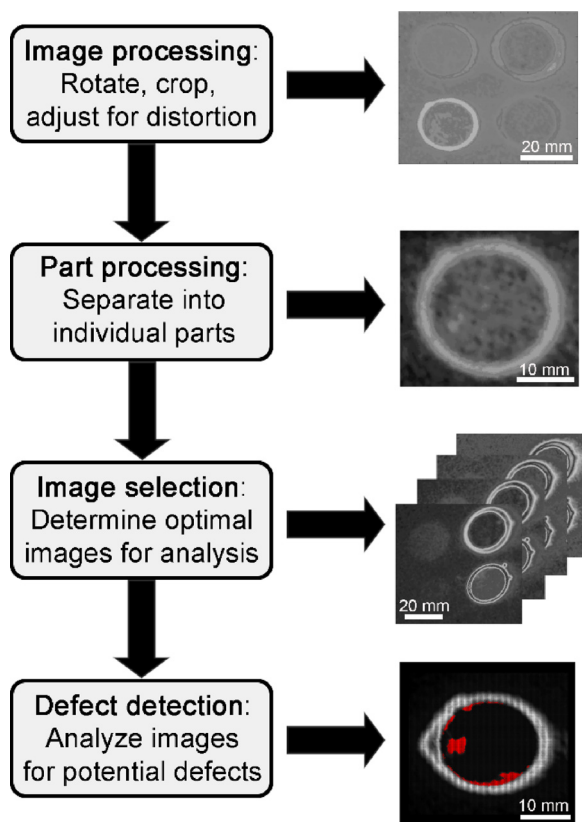


Fig. 2. Procedure for analyzing IR images acquired in-process and detecting thermal irregularities associated with the presence of defects.

direction, however this simplification is unlikely to affect the observed results at the part surface where cooling rates were large; the simplification is also justified by the fact that only relative temperature differences are of interest in the model results. The part sides and bottom

were held at 80 °C, simulating the retained heat in the surrounding powder bed and base plate. Though arbitrary, these temperature boundary conditions are appropriate approximate values for laser additive processes as determined experimentally [27,32]. The final layer was then added and heated to the material's melting point of 660 °C for 0.1 s and allowed to cool for 1 s. The material thermal conductivity was set as a function of temperature using the properties of cast A356 (with similar composition) from reference [33]. During cooling, the thermal distribution on the top surface with regards to the pore location was monitored. This modeling was performed solely to confirm that subsurface porosity will produce a measurable thermal signature at the surface of parts during additive manufacturing, not to calculate precise temperature distributions or characteristics of the signature. Because a commercial FE package was utilized with referenced boundary conditions and material properties, and because only *relative* temperatures were of interest, no further model validation was performed. Fig. 3 displays the meshed geometry, cutout defect, and the initial and boundary conditions of the model.

4. Results

With in-process layer-by-layer temperature distributions acquired throughout an entire SLM build, and defect detection strategies in place, we then assess the capabilities and accuracy of the IR system. The locations of *ex situ* identified defects, identified via SEM imaging, are compared with IR data obtained at the same locations and success rates are determined for each part. The mechanisms responsible for the formation of defects were not of interest to this study and were not evaluated; defects were produced and characterized in order to evaluate IR system detection capabilities. We additionally note that in the specimens produced, only lack of fusion defects were observed in three of the specimens (with the exception of the “keyhole melting” part), where the frequency and size of LoF defects differed between them. Thus, the sensor capabilities are assessed for LoF defects and for keyhole defects in SLM parts in this work. Furthermore, the determination that a large number of LoF defects remained in the baseline parts using optimal process parameters (as established by a full time SLM production

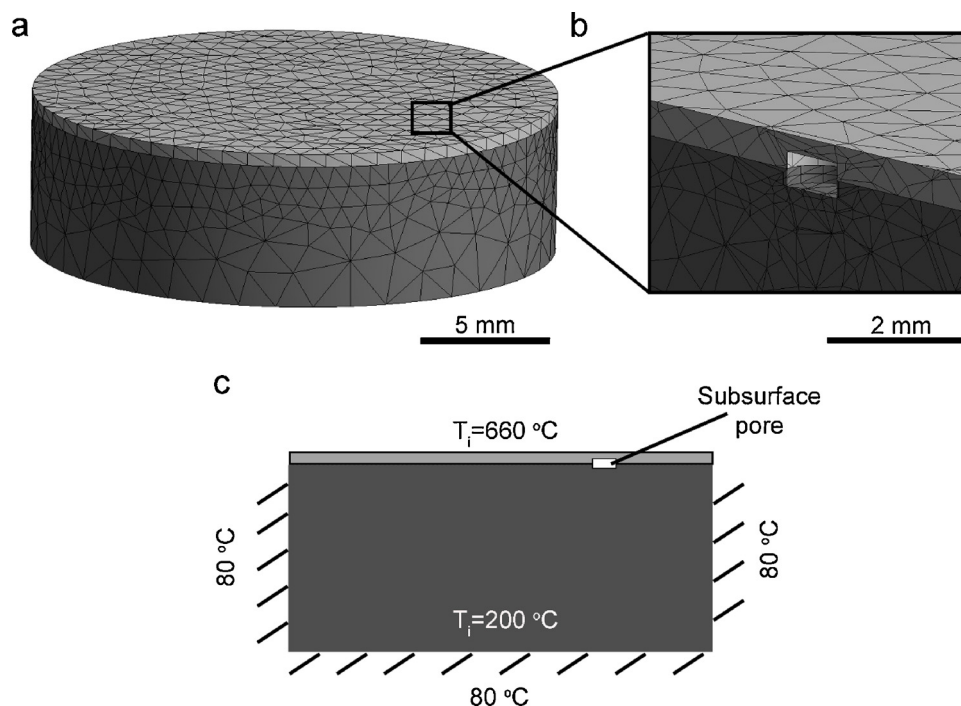


Fig. 3. Thermal modeling geometry and conditions. a) overview of meshed geometry, b) close-up of modeled porosity and c) thermal boundary conditions applied in model solution.

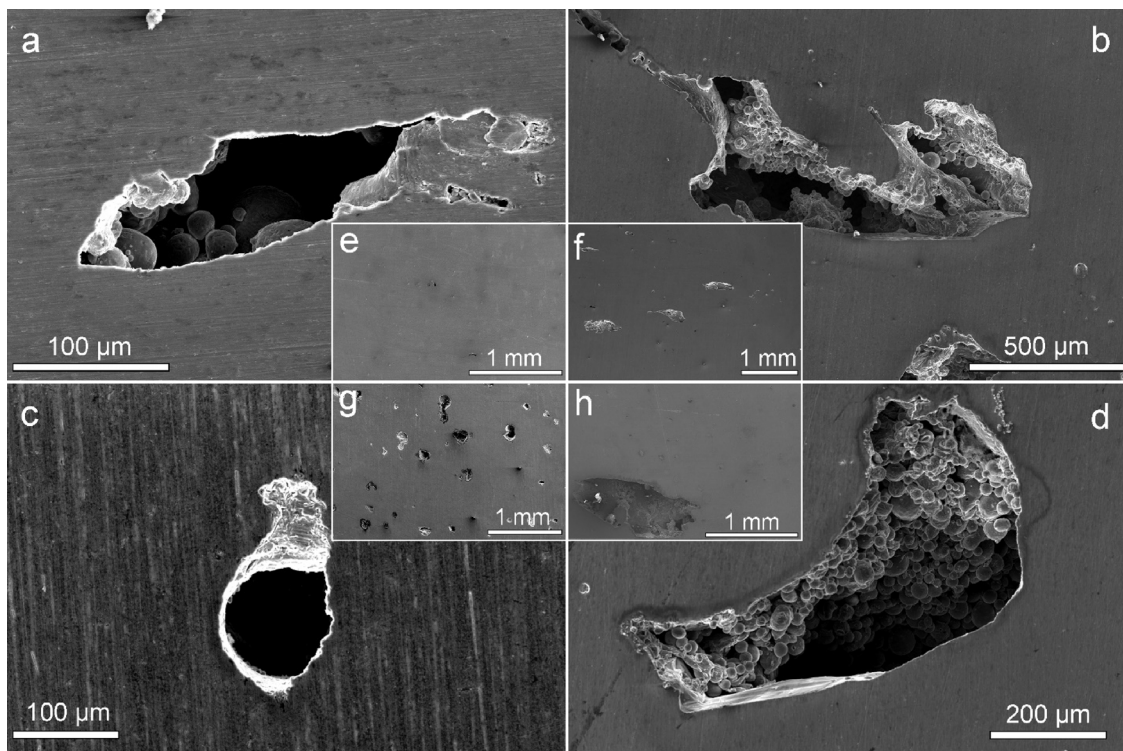


Fig. 4. Characteristic defects observed in each of the four produced SLM specimens, inset images show representative microstructure and defect population in each specimen at lower magnification: a) “Baseline” parameters, b) “Lack of Fusion-1” parameters, c) “Keyhole Melting” parameters and d) “Lack of Fusion-2” parameters.

facility) reinforces the necessity for an effective in-process monitoring system to detect and quantify such defects.

4.1. Characterization of AlSi10Mg defects

Fig. 4 shows characteristic defects observed in each of the four parts (produced with the distinct laser parameters described in Table 2) and micrographs of the macroscale microstructures. As noted, we observed that every part with the exception of the “keyhole melting parameter” part contained only LoF defects, with variations in size and quantity. The “Baseline Parameter” part (Fig. 4a/e) contained a moderate number of LoF defects on each sectioned plane and were generally in the range of 50–200 μm in the largest dimension (aligned perpendicular to the build direction). The “Lack of Fusion-1” parameter part (Fig. 4b/f) contained a large number of large LoF defects generally between 500 μm – 1.5 mm in the largest dimension. The “Lack of Fusion-2” part (Fig. 4d/h), was found to contain a small number of very large LoF defects on the order of 500 μm – 2 mm in the largest dimension. We note a large amount of spattering was indeed observed in this specimen in-process, while no spattering was observed visually in the other specimens. The result of this spattering was to produce several large lack of fusion defects; the different mechanisms of defect formation in each specimen were not of interest to this study and were not evaluated, the primary goal in producing the various specimens was to produce a range of defect sizes and distributions, and thus no further discussions of spattering or mechanics of defect formation will be made.

Contrastingly, the “Keyhole Melting” parameter set resulted in a part with only keyhole porosity (Fig. 4c/g). The pores were typically on the order of 100 μm in the largest dimension, which was aligned roughly parallel to the build direction; an excessive number of these pores were observed on each sectioned plane. We observed that no keyhole pores were formed within 150 μm from the top surface of the part, indicating that in-process these pores formed several layers below the layer being rastered, due to the high laser power and extremely slow scan rate. The geometry (size and shape) of the LoF defects, even

in the baseline (optimal) parameter part, indicates these defects would be highly detrimental to mechanical performance, specifically toughness and fatigue life. The sharp edges of these large defects will serve as strong stress concentration and crack initiation sites under loading. Additionally, many of the defects already featured small cracks at these sharp edges, likely formed during continued reheating and contraction caused during the deposition of subsequent layers. Thus, these defects are critically important to detect and limit in SLM parts to improve part quality and properties. We also have observed in SEM imaging that in many cases defects preferentially formed in the same x, y position in the parts (stacked vertically in the build direction) indicating that either 1) the presence of defects in underlying layers affected and promoted continued defect growth in subsequent layers at that location or 2) process anomalies such as powder spreading deficiencies or laser raster errors tended to occur at specific locations more frequently. This result highlights the need to identify defects in-process and to ultimately apply corrective actions at the first occurrence in order to alleviate systematic processing errors.

4.2. IR identification of defects

The IR anomaly detection strategy developed and applied in this study was able to identify defects with a high degree of success. Anomalies in infrared irradiance were easily detected and mapped in the analysis program (Fig. 5). By detecting and outlining anomaly geometry layer-by-layer, we successfully reproduced the 3-dimensional geometry of thermal irregularities in each part, which can then be plotted within the part geometry to better understand spatial dependence of the thermal anomalies. Furthermore, the IR imaging method (while using only relative temperatures) is quantitative in nature and allowed for the distinction between anomalies with high or low irradiance. Fig. 6 displays the 3D position and geometry of detected anomalies which are either 1 standard deviation above the mean temperature (Fig. 6a) or 1 standard deviation below the mean temperature (Fig. 6b) for the Lack of Fusion-1 parameter set part. We observe for this

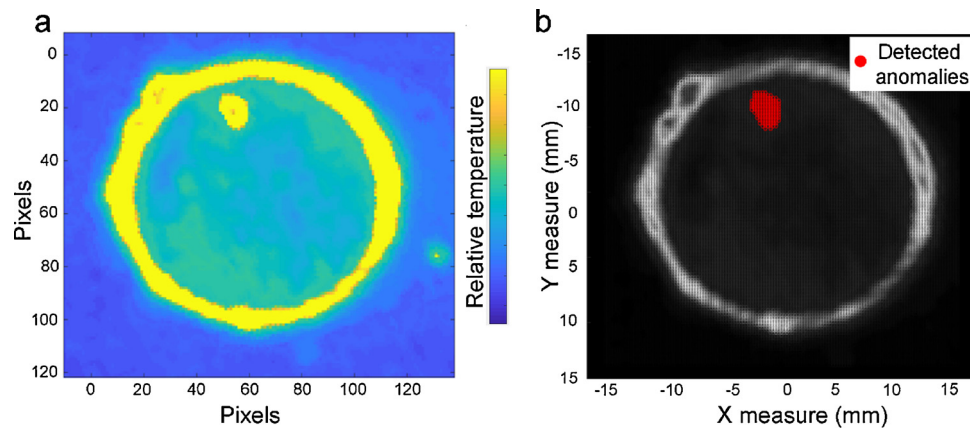


Fig. 5. a) Example of a thermal anomaly seen in IR imaging and b) the anomaly detected and outlined via defect detection program in post-processing.

“Lack of Fusion-1” part (which exhibited only LoF defects) a far greater number of IR anomalies with irradiance above the mean value (Fig. 6a) compared to anomalies below the mean (Fig. 6b). This result validates our original hypothesis that the subsurface porosity with unsintered powder would result in retained heat and hence a localized increase in IR signature at the surface.

We further use this quantitative data, which provided full spatial positioning of anomalies, to analyze the location dependence of defect formation in the parts. Fig. 7 displays histograms of the x-position (Fig. 7a) and y-position (Fig. 7b) dependencies of detected thermal anomalies within all four parts; the results show the total number of anomalous pixels at each location through every layer. Note that due to the circular geometry of the parts there is less cross-sectional length in the parts for a given x/y value moving away from the center of the part (the cross-section length decreases quadratically moving from the part center), therefore the histograms have been normalized by this cross-sectional length at every x/y position; thus, the histograms display defect concentration (number of anomalies per unit length) at each x/y location. Through this normalization, a completely random distribution of anomalies would result in a straight line across the histogram. There are several noticeable observations of the data in both x and y directions (refer to Fig. 1 for part locations, Fig. 7 inset shows the raster pattern and powder spread direction relative to coordinate system). In the x-direction we observe location dependencies that are clearly shared between multiple parts. For example, there are peaks in anomaly occurrences near $x = -7$ mm and $x = 3$ mm which is observed independently for three of the parts. This is an important result that indicates a macroscopic process irregularity occurred. The three parts

with LoF defects (all but the “keyhole parameter” part) were shown to have significant dependence on the x-position, while the keyhole melting specimen was observed to be relatively uniform through the x-direction. This result indicates that LoF development was strongly tied to geometry and powder spreading, while keyhole defects were essentially immune to these errors. Another important result is seen from the “baseline parameter” part: the concentration of anomalies was seen to increase as the x-position increased, i.e. as the recoater blade traversed the part surface more defects were found to form with its increased travel distance. The y-direction shows a similar trend of common locations of anomaly development between the parts. However, in this case the peaks are found solely at the outer edge positions for all parts produced; anomaly density through the central region of the specimens remained relatively uniform, in stark contrast to the x-direction results.

Next, we analyze the accuracy of the IR detected anomalies in predicting defect locations. This was accomplished by comparing the SEM characterization of defects to IR anomaly positions. We first create “virtual cross sections” of the 3D anomaly locations for a given part (Fig. 8a) which correspond to the sectioned planes used physically for SEM characterization. The sensor data can then be compared directly to SEM identified defects, by marking defect positions during imaging. 3 cross sectional planes were imaged for each part, with a minimum of 3–5 defects being imaged and spatially marked for each plane. In the three LoF producing specimens, approximately 10–15 defects of varying size were generally observed in each cross-section during SEM imaging. The “keyhole parameter” specimen exhibited excessive porosity, generally with greater than 50 defects per cross-section. The IR anomaly data correlated very strongly with LoF defects observed in the parts

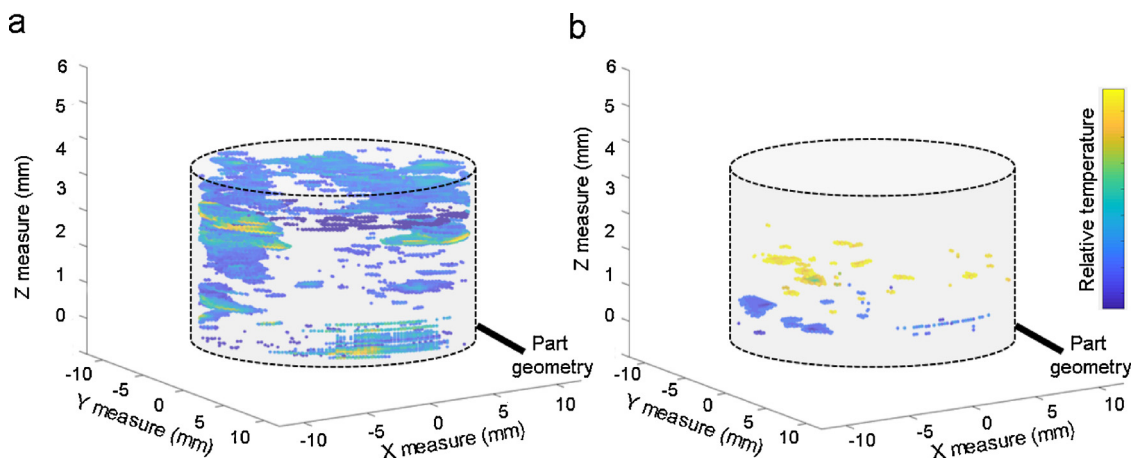


Fig. 6. Thermal irregularities detected within the “Lack of Fusion” parameter part. a) Thermal irregularities with higher than average irradiance and b) thermal irregularities with lower than average irradiance.

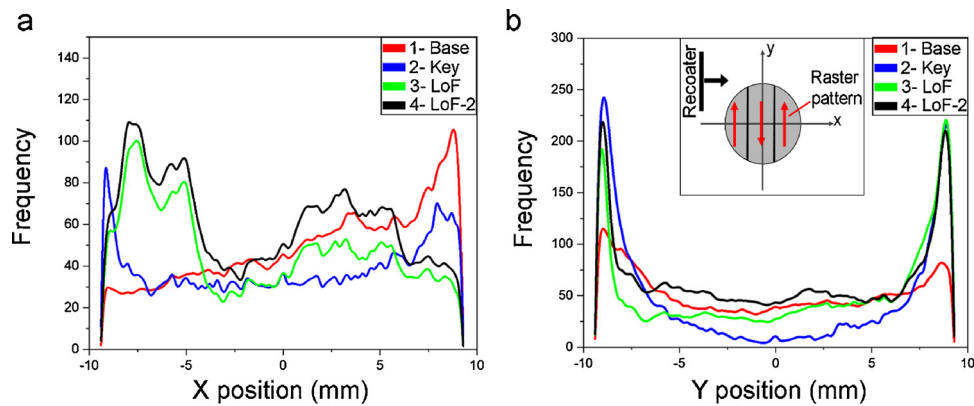


Fig. 7. Histograms of thermal anomaly location dependence in a) X- and b) Y- coordinates. Note the origin (0, 0) corresponds to the center of each part. Inset shows raster orientation, recoater motion and part coordinate system.

(Fig. 8), where defect position, relative locations to other defects, and approximate geometry was recreated well in the IR data for most cases. This type of comparison between IR data virtual planes and SEM imaged defects (Fig. 8) was performed for each marked defect, on every imaged plane of each specimen. The defect was marked as successfully identified by IR data only if an IR anomaly was found within ± 0.1 mm of the marked physical defect location (allowing for a small degree of measurement error). We note that the size scale of thermal anomalies detected via IR imaging was generally larger than the physical size of defects, due to the conduction of retained heat around the defect location; i.e. a LoF defect 100 μm in size may produce a unique thermal signature (of increased temperature) on the order of 200–500 μm on the surface. A similar result is observed in thermal modeling (Section 4.3).

We observed very strong correlation between IR data and physical defects for each of the parts with LoF defects. In total, between all observed LoF defects, an 82% success rate was achieved for identifying physical defect locations from IR data. Keyhole melting, however, was less successfully captured via this full-field IR methodology, with a success rate of only 33%. A contributing factor to this poor success rate is the location of the defects that formed. As mentioned in Section 4.1, no keyhole pores were observed within 150 μm of the part surface, indicating that these defects were formed several layers below the imaged layer. This fact likely prohibited their detection via surface IR imaging. The success rate in correlating IR anomalies with physical defects for each part, along with the total number of defects analyzed per sample, is given in Table 3. Note in samples (such as the Lack of Fusion-1 parameter set) that contained a large number of defects, a sample group of defects were randomly selected during SEM imaging at distant points on the plane (not in a single concentrated area) for comparison to IR data; the IR data was not referred to beforehand or

Table 3
Success rates in correlating *ex situ* identified defects to in-process IR identified anomalies by each part produced and by defect type.

Part	Detection success rate	# Defects analyzed
“Baseline”	78%	14
“Keyhole”	33%	12
“Lack of Fusion-1”	80%	15
“Lack of Fusion-2”	88%	16
Defect type	Detection success rate	Total # by type
LoF total	82%	45
Keyhole total	33%	12

used as a guide in defect selection in any way. Finally, the success of detecting LoF defects was analyzed based on the size of the defects observed. This comparison was enabled by the wide distribution of LoF defect sizes observed between the Lack of Fusion-1, Baseline and Lack of Fusion-2 parameter set specimens. The lateral dimension of each imaged defect was recorded, and its representation in IR data analyzed. Fig. 9 shows the results of this size dependence analysis. We observed a strong (approximately linear) relationship between defect size and the ability to detect the defect via IR imaging. As the defect size increases, the IR measurements become more likely to detect them. This is an expected result and indicates the spatial resolution of the IR camera likely played a crucial role in limiting the critical detectable defect size. Defects below approximately 50 μm were only detected with a 50% success rate. Contrastingly, defects larger than 500 μm were detected via IR data with 100% accuracy in this sample group. Note these are the results of the observed (SEM imaged) defects and represents a random sample group of all defects in

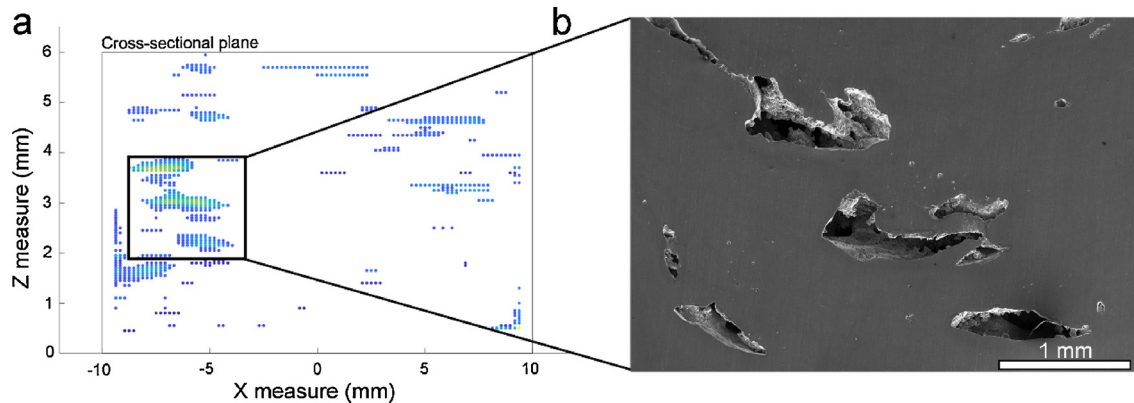


Fig. 8. a) IR detected defects on a sectioned plane compared to b) SEM imaged defects at the same location. Note number, size, and location of defects matched favorably between IR data and physical defects.

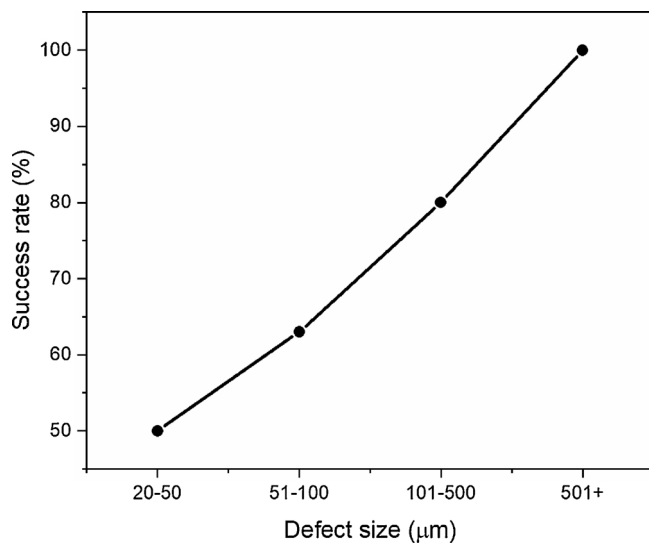


Fig. 9. Defect detection success rate for LoF defects via IR thermography versus physical defect size range.

the specimens; not all defects present on each sectioned plane were considered/imaged.

4.3. Thermal modeling of defect signatures

Thermal modeling strongly supported the results observed via IR imaging. Namely, the model confirmed that a defect centered at the bottom of a given layer would leave a detectable thermal signature at the surface (Fig. 10). The model also validated the result that IR detected thermal anomalies were much larger than the size of the physical defect which produced it. The 1 mm defect used in modeling resulted in a thermal signature at the surface (with temperatures 1 standard deviation above the mean temperature) roughly ~2.5 mm in diameter immediately following the removal of the melt condition. We also note in modeling that the thermal signature dissipated entirely within 0.5 s and returned to a roughly axisymmetric distribution. In-process, thermal irregularities were observed in IR imaging to remain for a much longer duration. This is likely the result of the simplicity of the computational modeling, where only a single layer was added and an arbitrary equilibrium temperature was given to the underlying part. However, the modeling served to validate the important results

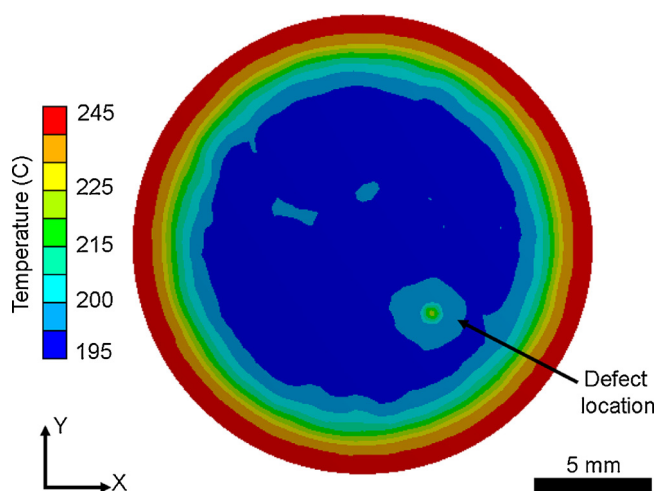


Fig. 10. Temperature distribution on part surface produced via thermal modeling. Subsurface defect resulted in a large, detectable, thermal signature on the part surface.

observed in IR data. Namely, that subsurface porosity leaves a detectable thermal signature on the part surface, and that this thermal signature at the part surface is significantly larger than the physical dimensions of the defect. We believe this result (observed both in modeling and experimentally) critically enabled the detection of physical defects below the spatial resolution of the IR camera. With an approximate field of view of 250 mm x 250 mm, and the known image resolution of the camera, each pixel represented a surface area of approximately 195 μm x 260 μm. Therefore, the detection of defects below 100 μm in size (Fig. 9) was enabled by this fact that the thermal signature was much larger than the defect itself; this represents an inherent benefit to process monitoring through thermal imaging in that defects below the spatial resolution may still be detected.

5. Discussion

The results in this study strongly indicate that it is possible to detect subsurface lack of fusion defects in SLM parts, *in situ*, via full-field infrared thermography. Lack of fusion defects may be the most critically debilitating to SLM part performance. These defects are often very large, irregularly shaped, filled with un-sintered powder and feature sharp edges. The geometry of these defects will dramatically affect fatigue life, where the sharp boundaries will serve as prime crack initiation sites. Furthermore, many defects were observed to have microcracks at these edges already; these cracks will thus propagate during cyclic loading and dramatically reduce fatigue life. Additionally, the presence of un-sintered powder and branched microcracks will likely prevent complete alleviation by hot isostatic pressing (HIP) post-processing methods. Therefore, the detection of these defects during SLM processing is critically important to effective part qualification. Furthermore, the fact that the “baseline parameter” specimens (produced using optimized processing parameters) exhibited only LoF defects reinforces the importance of developing methods to detect these defects and indicates that special emphasis should be placed on targeting this defect type, in the presently studied aluminum alloy. The developed IR monitoring strategy and analysis method successfully detected 82% of these LoF defects. Large LoF defects were detected with a high degree of accuracy via this method (100% for defects above 0.5 mm). This result has two important implications: 1) larger defects, which will be more critical to detect, inherently have a higher probability of being detected in-process and 2) the spatial resolution of the IR camera likely plays a large role in determining the minimum detectable defect size, hence higher resolution imaging can likely further improve defect detection capabilities through this method. The full-field imaging strategy and analysis differs significantly from the majority of other IR studies in the literature, which have primarily focused on melt pool monitoring. The results of this study indicate that real-time defect detection, for LoF defects, in SLM processing can be achieved by facile full-field monitoring of surface irradiance. This method has several important advantages: 1) machine integration is simple and quickly accomplished, no custom optics or modification to the machine is necessary and the camera can be removed or adjusted easily, 2) using only relative temperatures eliminates the need for difficult emissivity calibration/corrections which are material and temperature dependent and 3) quantitative data can be acquired regarding defect position, size and geometry. The difficulty in detecting keyhole porosity should be further studied to assess feasibility. In this study it is apparent that the extremely slow scan rate and high laser power resulted in keyhole pores being formed several layers below the surface, which ultimately resulted in the thermal signature of keyhole pores being undetectable via IR imaging.

It is also important to discuss at this juncture the importance of the criterion for defining “irregularity” in the thermal images. In this work, an irradiance value of ± 1 standard deviation away from the mean was selected to mark abnormal pixels corresponding to subsurface defects. This value was selected based on the easily understood definition of

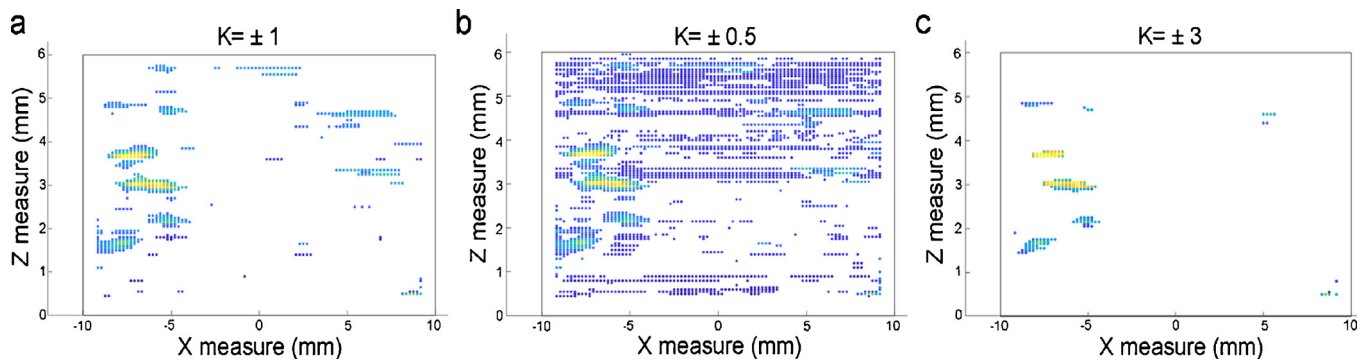


Fig. 11. Demonstration of defect identification sensitivity to the value of selected abnormality criterion (units of standard deviation away from mean): a) $K = \pm 1$ standard deviation (value used in this work), b) $K = \pm 0.5$ standard deviations and c) $K = \pm 3$ standard deviations.

being a standard unit outside the norm, which allowed for rigid identification protocols to be established. However, continuing towards real-time defect detection and optimization, further studies should be conducted to determine the optimal criterion for defining “abnormality”. Here, we briefly demonstrate the importance of this value to the results through a sensitivity study. Fig. 11 displays the same cross-sectional plane of IR data given in Fig. 8 as it changes with alterations to the selection criterion (i.e. $\pm K$ standard deviation units). We see that with a reduction in the criterion ($K < 1$) more abnormal pixels will be defined, leading to a plethora of likely erroneous identifications not representing true physical defects (Fig. 11b). Contrastingly, we can see that an increase in the criterion ($K > 1$) reduces the number of abnormal points identified, potentially missing physical defects (Fig. 11c). In further studies, this criterion for defining thermal irregularity may be better optimized to identify the highest possible percentage of true defects.

The ability to acquire spatial position data for all thermal irregularities in SLM parts also resulted in the unique ability to analyze process consistency. The distribution of irregularities with regards to (x/y) position in the parts demonstrated that process irregularities were repeated in preferential locations and provided another intriguing route to understanding SLM process deficiencies. In general, the spatial dependence of thermal irregularity/defect development would likely indicate that either: 1) the presence of underlying defects at a location influences further defect development in subsequent layers, 2) laser irregularities (such as raster turning points or laser profiling at given points) resulted in defect formation at preferred locations or 3) macroscopic processing conditions resulted in preferred defect formation locations (e.g. part geometry or powder spreading deficiencies likely caused by recoater blade inconsistencies). Given the shared anomaly dependence in the x-direction between multiple parts (Fig. 7a), we may more strongly assume that a macroscopic process irregularity occurred which led to defect formation at these locations in each part. It is likely that interactions between the recoater blade and part geometry, where spreading errors occurred, contributed strongly to this spatial dependence of anomalies. In-process, the recoater blade was observed to interact with the surface at certain points leading to intermittent motion of the blade (i.e. the blade frequently skipped over the surface at certain points) across the entire powder bed (Fig. 12a), which would likely lead to the preferential production of defects at certain positions shared by multiple parts. We additionally observe in SEM imaging that defects tended to form in the same x,y position in parts at multiple layers throughout a build (Fig. 12b), suggesting that these defects resulted due to a recurring systematic process error, which was identically observed in the IR anomaly data. The y-position dependence of detected anomalies may also be considered with regards to the raster pattern and powder spread direction (Fig. 7 inset). The y-direction is the lengthwise direction of the primary laser raster for every layer, thus at extreme y-values is where the raster is beginning and ending, which may result in

an increase of defect density, since full laser melt conditions have not yet been established. The uniformity in defect concentration through the central portion of all parts in the y-direction (in direct contrast to the x-position dependence) again indicates that the recoating process directly influenced defect formation. Because the recoater blade is parallel to the established y-axis, we would expect a uniform distribution in this direction, as was observed for all produced parts. It is understood that LoF defects may preferentially form near the edge of raster tracks, where sufficient track overlap is necessary to ensure removal of these defects [7]. However, this phenomenon does not explain the global position dependence of defects observed in these results; since the raster pattern was translated horizontally between each layer through the build, we would not expect this effect to cause an unusual density of defects at few discrete locations. We therefore conclude that other systematic process errors were the cause of this observed location dependence. The lack of position dependence in anomaly formation for the “keyhole melting part” (Fig. 7) further implies that these recurring process errors, likely powder spreading errors, result in LoF defects under standard laser parameters, but are eliminated by the high laser power and slow scan speeds used in this specimen that resulted only in keyhole porosity. These analyses highlight the capability of the developed IR methodology to identify process defects and to assess process consistency and likely contributing factors in defect development.

6. Conclusions

This study has provided new answers to the critical questions surrounding IR monitoring in SLM processing that were posed in Section 1. Namely, the current study demonstrated successful IR monitoring and unique analysis methods that resulted in effective detection of lack of fusion defects in SLM parts; 82% of characterized LoF defects were determined to be effectively detected via IR imaging, demonstrating that IR thermal signatures do in fact correlate well with physical material defects. Defect size was found to be the critical factor in detectability via IR imaging; defects above 0.5 mm were represented in IR data with 100% success in this sample group, while defects below 50 μm were detected only 50% of the time. Improving IR spatial resolution/camera positioning may further improve detection for small defects. The 3D spatial positions of defects in produced parts were acquired through this method, and approximate defect size/geometry could be analyzed. The thermal signature of LoF defects (the IR signature analyzed) was determined to be roughly 2–5 times the size of the physical defect, which was supported by computational modeling; this fact also enabled the detection of defects below the pixel size of IR images. This relationship is a function of part geometry, material thermal conductivity, processing conditions and layer height, and requires further investigation to accurately determine physical defect size from IR imaging. It was determined that, in this study, keyhole porosity was not detected effectively via full-field IR monitoring, with a success

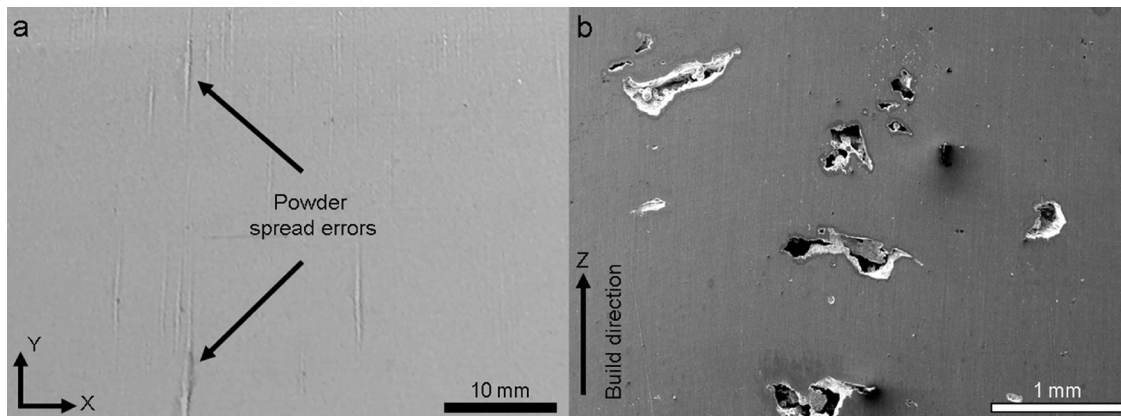


Fig. 12. Examples of preferential formation of defects at a given position: a) Photograph captured in-process of powder spreading errors prior to rastering located at a common X-location through the powder bed caused by the recoater blade-part interaction and b) SEM image of defects formed at the same x,y (in-plane) position at multiple layers through the build.

rate of only 33%. This result is likely due to the specific processing conditions used in the experiment. Optimization of the “abnormality criterion”, i.e. the metric used to mark a pixel as irregular (in this case ± 1 standard deviation from the mean), requires additional studies in order to ensure the highest percentage of defects are correctly identified. The ability to effectively map anomaly locations throughout the 3D geometry of SLM parts, as developed in this work, led to the ability to analyze SLM process consistency and to search for systematic processing errors, an analysis method and capability of IR process monitoring not reported elsewhere. With a better understanding of the results IR monitoring provides, and the capabilities of the method in detecting material defects, these types of analyses provided by full-field *in situ* IR monitoring can immediately lead to more effective SLM part qualification methods. Furthermore, the full-field detection strategy is high-throughput and could ultimately be implemented into a real-time control system to reduce or eliminate LoF defects during SLM production.

Acknowledgements

This work was performed as a joint effort between the University of Virginia and MC Technologies LLC. In-process SLM experiments were performed through a collaboration with Volunteer Aerospace Inc. in Knoxville, TN. We thank the University of Virginia NanoMaterials Characterization Facility (NMF) for providing access and support to SEM facilities. This research was partially funded by the U.S. Government (Army RDECOM) under contract No. W911W6-18-C-0005. The U.S. Government is authorized to reproduce and distribute reprints for Government purposes notwithstanding any copyright notation thereon. The views and conclusions contained in this document are those of the authors and should not be interpreted as representing the official policies, either expressed or implied, of the Aviation Development Directorate or the U.S. Government.

References

- [1] T. DebRoy, H.L. Wei, J.S. Zuback, T. Mukherjee, J.W. Elmer, J.O. Milewski, A.M. Beese, A. Wilson-Heid, A. De, W. Zhang, Additive manufacturing of metallic components – process, structure and properties, *Prog. Mater. Sci.* 92 (2018) 112–224.
- [2] D.D. Gu, W. Meiners, K. Wissenbach, R. Poprawe, Laser additive manufacturing of metallic components: materials, processes and mechanisms, *Int. Mater. Rev.* 57 (3) (2012) 133–164.
- [3] W.E. King, A.T. Anderson, R.M. Ferencz, N.E. Hodge, C. Kamath, S.A. Khairallah, A.M. Rubenchik, Laser powder bed fusion additive manufacturing of metals; physics, computational, and materials challenges, *Appl. Phys. Rev.* 2 (041304) (2015) 1–26.
- [4] A. Basak, S. Das, Epitaxy and microstructure evolution in metal additive manufacturing, *Annu. Rev. Mater. Res.* 46 (2016) 125–149.
- [5] P. Mercelis, J.P. Kruth, Residual stresses in selective laser sintering and selective laser melting, *Rapid Prototyp. J.* 12 (5) (2006) 254–265.
- [6] S. Leuders, M. Thöne, A. Riemer, T. Niendorf, T. Tröster, H.A. Richard, H.J. Maier, On the mechanical behaviour of titanium alloy TiAl6V4 manufactured by selective laser melting: Fatigue resistance and crack growth performance, *Int. J. Fatigue* 48 (2013) 300–307.
- [7] B. Zhang, Y. Li, Q. Bai, Defect formation mechanisms in selective laser melting: a review, *Chin. J. Mech. Eng.* 30 (2017) 515–527.
- [8] S.K. Everton, M. Hirsch, P. Stravroulakis, R.K. Leach, A.T. Clare, Review of in-situ process monitoring and in-situ metrology for metal additive manufacturing, *Mater. Des.* 95 (2016) 431–445.
- [9] W.E. King, H.D. Barth, V.M. Castillo, G.F. Gallegos, J.W. Gibbs, D.E. Hahn, C. Kamath, A.M. Rubenchik, Observation of keyhole-mode laser melting in laser powder-bed fusion additive manufacturing, *J. Mater. Process. Technol.* 214 (12) (2014) 2915–2925.
- [10] K. Darvish, Z.W. Chen, T. Pasang, Reducing lack of fusion during selective laser melting of CoCrMo alloy: Effect of laser power on geometrical features of tracks, *Mater. Des.* 112 (2016) 357–366.
- [11] T. Mukherjee, J.S. Zuback, A. De, T. Debroy, Printability of alloys for additive manufacturing, *Sci. Rep.* 6 (19717) (2016) 1–8.
- [12] H.D. Carlton, A. Haboub, G.F. Gallegos, D.Y. Parkinson, A.A. MacDowell, Damage evolution and failure mechanisms in additively manufactured stainless steel, *Mater. Sci. Eng. A* 651 (2016) 406–414.
- [13] H. Gong, K. Rafi, H. Gu, G.D.J. Ram, T. Starr, B. Stucker, Influence of defects on mechanical properties of Ti-6Al-4V components produced by selective laser melting and electron beam melting, *Mater. Des.* 86 (2015) 545–554.
- [14] G. Kasperovich, J. Haubrich, J. Gussone, G. Requena, Correlation between porosity and processing parameters in TiAl6V4 produced by selective laser melting, *Mater. Des.* 105 (2016) 160–170.
- [15] N.T. Aboulkhair, N.M. Everitt, I. Ashcroft, C. Tuck, Reducing porosity in AlSi10Mg parts processed by selective laser melting, *Addit. Manuf.* 1–4 (2014) 77–86.
- [16] C. Weingarten, D. Buchbinder, N. Pirch, W. Meiners, K. Wissenbach, R. Poprawe, Formation and reduction of hydrogen porosity during selective laser melting of AlSi10Mg, *J. Mater. Process. Technol.* 221 (2015) 112–120.
- [17] G. Tapia, A. Elwany, A review on process monitoring and control in metal-based additive manufacturing, *J. Manuf. Sci. Eng.* 136 (060801) (2014) 1–10.
- [18] S. Berumen, F. Bechmann, S. Lindner, J.P. Kruth, T. Craeghs, Quality control of laser- and powder bed-based Additive Manufacturing (AM) technologies, *Phys. Procedia* 5B (2010) 617–622.
- [19] S. Clijsters, T. Craeghs, S. Buls, K. Kempen, In situ quality control of the selective laser melting process using a high-speed, real-time melt pool monitoring system, *Int. J. Adv. Manuf. Technol.* 75 (2014) 1089–1101.
- [20] T. Craeghs, S. Clijsters, J.P. Kruth, F. Bechmann, M.C. Ebert, Detection of process failures in layerwise laser melting with optical process monitoring, *Phys. Procedia* 39 (2012) 753–759.
- [21] E. Rodriguez, J. Mireles, C.A. Terrazas, D. Espalin, M.A. Perez, R.B. Wicker, Approximation of absolute surface temperature measurements of powder bed fusion additive manufacturing technology using in situ infrared thermography, *Addit. Manuf.* 5 (2015) 31–39.
- [22] B. Cheng, S. Price, J. Lydon, K. Cooper, K. Chou, On process temperature in powder-bed electron beam additive manufacturing: model development and validation, *J. Manuf. Sci. Eng.* 136 (061018) (2014) 1–12.
- [23] F. Bayle, M. Doubenskaia, Selective laser melting process monitoring with high speed infra-red camera and pyrometer, *Proc. SPIE* 6985 (698505) (2008) 1–8.
- [24] P. Lott, H. Schleifenbaum, W. Meiners, K. Wissenbach, C. Hinke, J. Bültmann, Design of an optical system for the in situ process monitoring of selective laser melting (SLM), *Phys. Procedia* 12A (2011) 683–690.
- [25] G. Zenzinger, J. Bamberg, A. Ladewig, T. Hess, B. Henkel, W. Satzger, Process monitoring of additive manufacturing by using optical tomography, *AIP Conference Proceedings* 1650 (2015) 164–170.

- [26] S. Kleszczynski, J. zur Jacobsmuhlen, J.T. Sehr, G. Witt, Error detection in laser beam melting systems by high resolution imaging, *Solid Freeform Fabrication Symposium 23* (2012) 975–987.
- [27] E.R. Denlinger, J.C. Heigel, P. Michaleris, T.A. Palmer, Effect of inter-layer dwell time on distortion and residual stress in additive manufacturing of titanium and nickel alloys, *J. Mater. Process. Technol.* 215 (2015) 123–131.
- [28] A.J. Dunbar, E.R. Denlinger, J. Heigel, P. Michaleris, P. Guerrier, R. Martukanitz, T.W. Simpson, Development of experimental method for in situ distortion and temperature measurements during the laser powder bed fusion additive manufacturing process, *Addit. Manuf.* 12A (2016) 25–30.
- [29] J. Raplee, A. Plotkowski, M.M. Kirka, R. Dinwiddie, A. Okello, R.R. Dehoff, S.S. Babu, Thermographic microstructure monitoring in electron beam additive manufacturing, *Sci. Rep.* 7 (43554) (2017) 1–16.
- [30] Y. Ding, J. Muñoz-Lerma, M. Trask, S. Chou, A. Walker, M. Brochu, Microstructure and mechanical property considerations in additive manufacturing of aluminum alloys, *MRS Bull.* 41 (10) (2016) 745–751.
- [31] K. Kempen, L. Thijs, J.V. Hunbeeck, J.P. Kruth, Mechanical properties of AlSi10Mg produced by selective laser melting, *Phys. Procedia* 39 (2012) 439–446.
- [32] A.J. Dunbar, E.R. Denlinger, M.F. Gouge, T.W. Simpson, P. Michaleris, Comparisons of laser powder bed fusion additive manufacturing builds through experimental in situ distortion and temperature measurements, *Addit. Manuf.* 15 (2017) 57–65.
- [33] R. Overfelt, S.I. Bakhtiyarov, R.E. Taylor, *Thermophysical Properties of A201, A319, and A356 Aluminium Casting Alloys High Temp.* 34 High Press, 2002, pp. 401–409.